Applied Thermal Engineering 257 (2024) 124321

Contents lists available at ScienceDirect

Applied Thermal Engineering

journal homepage: www.elsevier.com/locate/apthermeng

Research Paper

CFD-based shape optimization of flashing converging-diverging nozzles in pelton turbines for domestic carbon dioxide heat pumps including off-design conditions

Kiavash Kamali, Paolo Gaetani, Giacomo Persico, Alessandro Romei *

Laboratory of Fluid Machines, Department of Energy, Politecnico di Milano, Via Lambruschini 4a, Milano 20156, Italy

A B S T R A C T

A path to enhance the coefficient of performance (COP) of domestic heat pumps is to replace the throttling valve with a turboexpander. Designing this component requires addressing supersonic flashing flows localized within the nozzle. In particular, two-phase flows prevent the application of the method of characteristics to design efficient converging–diverging shapes. To overcome this issue, we propose a shape optimization combined with a homogeneous equilibrium flow model as a design tool. Kriging models are used as surrogates of the objective function and constraint to reduce the overall computational burden associated with shape optimization. The infilling criterion to improve surrogate accuracy involves the maximization of the constrained expected improvement. A multi-point optimization is formulated, including design and off-design conditions in both objective and constraint, for a total of four relevant operating conditions. The off-design conditions are derived from system analysis, accounting for variations in the evaporator temperature and outlet gas-cooler temperature. The optimized nozzle results in a COP improvement of 7.6%, compared to a 6.6% increase when replacing the throttling valve with a baseline geometry designed as recommended by the literature. The adoption of a multi-point optimization strategy ensures that this enhancement in design conditions is not offset by off-design performance decay, which is 0.3 percentage points over the three off-design conditions. Overall, replacing the throttling valve with the optimized expander leads to an average COP improvement of 8.6%.

1. Introduction

As sustainable development emerges as the guiding principle for the future, energy and environmental concerns have garnered heightened attention over the past decade. Among the most energy-intensive sectors, the building industry stands out prominently [1,2]. The demand for heating and hot water contributes significantly to energy consumption, traditionally met by fossil fuel combustion or electric heating methods. However, the emergence of renewable energy sources has shifted the focus toward heat pumps, which have gained widespread attention. Heat pumps are increasingly popular due to their ability to facilitate building electrification, thereby enhancing the utilization of renewable energy resources. Air-source heat pumps (ASHPs) have demonstrated their competitiveness as a technical solution for water heating systems owing to their notable attributes, including high energy efficiency, low capital cost, safety, and convenience [3].

According to the Montreal Protocol, there is a mandate to gradually phase out the consumption and production of synthetic refrigerants like R22 and R410a, thereby emphasizing the pressing need to adopt environmentally friendly alternatives [4]. Carbon dioxide (CO_2), classified as a natural refrigerant, has gained significant attention in recent years due to its numerous advantageous characteristics, including its low global warming potential, zero ozone depletion potential, low toxicity, and minimal flammability, which distinguish it from other refrigerants [5]. Despite its advantageous characteristics, CO_2 exhibits a lower critical temperature (31 °C) compared to most conventional refrigerants. This limitation imposes a restricted temperature range at the sink side of the cycle, particularly when employed CO_2 in a subcritical cycle. Lorentzen et al. [6–8] proposed the transcritical CO_2 cycle as an innovative approach to overcome this challenge, aiming to expand the operational range and enhance the overall performance of the thermodynamic cycle.

The significant pressure variation during the expansion of refrigerant in a transcritical CO_2 cycle results in considerable throttling losses, contributing to lower cycle efficiency compared to subcritical cycles using conventional HCFC refrigerants [9]. To enhance the competitiveness of CO_2 heat pumps, researchers suggest employing an ejector to elevate compressor suction pressure, thereby improving the cycle coefficient of performance (COP) [10–12]. Although two-phase ejectors offer relatively modest efficiency potential, a few commercially available ejectors have been incorporated into CO_2 heat pump water heaters in recent years [13]. The alternative approach involves replacing the conventional throttling valve with an expander to recover a portion of

* Corresponding author.
E-mail address: alessandro.romei@polimi.it (A. Romei).

https://doi.org/10.1016/j.applthermaleng.2024.124321
Received 12 April 2024; Received in revised form 19 July 2024; Accepted 2 September 2024
Available online 3 September 2024

Nomenclature

Acronyms

ASHP	Air-source heat pump
CFD	Computational fluid dynamic
COP	Coefficient of performance
CP	Control point
DE	Differential evolution
DoE	Design of experiments
EI	Expected improvement
GCI	Grid convergence index
HEM	Homogeneous equilibrium model
LHS	Latin hypercube sampling
LUT	Look-up table
MoCs	Method of characteristics
NRMSE	Normalized root mean squared error
STD	Standard deviation
WMAPE	Weighted mean absolute percentage error
CO_2	Carbon dioxide

Greek symbols

ε	L_2- norm of control points position (mm)
η	Efficiency
θ	Diverging angle (deg)
ρ	Density $\left(\mathrm{kg\ m^{-3}}\right)$
Φ	Cumulative distribution function
ϕ	Probability density function
ψ	Key variable
ω	turbulent kinetic energy dissipation rate $\left(\mathrm{m^2\ s^{-3}}\right)$

Roman symbols

a_i	i^{th} control point
D	Diameter (mm)
$\mathbb{E}[I(\boldsymbol{x})]$	Expected improvement function
$\mathbb{E}_c[I(\boldsymbol{x})]$	Constrained expected improvement
e_a	Approximated relative error
e_{ext}	Extrapolated relative error
F_{obj}	Optimization objective function
$g(\boldsymbol{x})$	Constraint function
$\widehat{g}(\boldsymbol{x})$	Kriging prediction for constraint function
h	Specific enthalpy $\left(\mathrm{kJ\ kg^{-1}}\right)$
k	Turbulent kinetic energy $\left(\mathrm{m^2\ s^{-2}}\right)$
k_p	Pelton wheel velocity ratio
L	Nozzle length (mm)
$\dot{m}$	Mass flow rate $\left(\mathrm{g\ s^{-1}}\right)$
N_{CP}	Number of control points
N_{test}	Number of testing data samples
n_{comp}	Compressor speed (rpm)
$\mathbb{P}[g(\boldsymbol{x}) < g_{max}]$	Probability distribution function
P	Pressure (bar)
$\mathscr{P}$	Apparent order of method
$\dot{Q}$	Thermal Power (kW)
R	Radius (mm)
r	Radial distance (mm)
r^2	Coefficient of determination
S	Surface area $\left(\mathrm{mm^2}\right)$
s	Specific entropy $\left(\mathrm{J\ kg^{-1}\ K^{-1}}\right)$
$\widehat{s}(\boldsymbol{x})$	Prediction uncertainty
$\widehat{s}_g(\boldsymbol{x})$	Constraint function prediction uncertainty
T	Temperature ($^\circ$C)
U	Pelton wheel peripheral speed $\left(\mathrm{m\ s^{-1}}\right)$
V	Flow velocity $\left(\mathrm{m\ s^{-1}}\right)$
$\dot{W}_{comp}$	Compressor power (kW)
$\boldsymbol{x}$	Vector of design input variables
y	Objective function value
y^+	Dimensionless wall distance
y_{min}	Objective function best value from CFD
$\widehat{y}(\boldsymbol{x})$	Kriging prediction for objective function
z	Axial distance (mm)

Subscripts and superscripts

amb	Ambient
ax	Axis
base	Baseline nozzle
conv	Nozzle converging section
CP	Control point
cr	Thermodynamic critical point
des	Designed value
div	Nozzle diverging section
eva	Evaporator
exp	Expander
ext	Extrapolated value
gc	Gas cooler
I	Initial sample data set
in	Inlet
is	Isentropic evolution
jet	Nozzle jet
mass	Mass flow rate based
max	Maximum value
min	Minimum value
noz	Nozzle
op	Operating condition
opt	Optimized
out	Outlet
ref	Reference value
sh	Superheating
$\overline{S}_z$	Evaluation surface
t	Total quantity
test	Test dataset
th	Nozzle throat
vel	Velocity
w	Water
wheel	Pelton wheel

the expansion work. Positive displacement expanders have seen extensive development in CO_2 refrigeration cycles and demonstrated commendable efficiencies [14–18]. Nickl et al. [18] devised and experimentally tested a piston compressor-expander unit for refrigeration systems with power sizes of $4-40$ kW, achieving an isentropic expansion efficiency ranging from 65% to 70%. This led to a cycle COP improvement of at least 40% compared to the throttled cycle. Du et al. [19], conducted a comprehensive review of micro-scale expanders (<200 kW) for CO_2-based power and refrigeration cycles. Their findings indicate that scroll, vane, and piston expanders are the primary contenders for refrigeration cycles. The authors highlight scroll and vane expanders as particularly promising due to their independence from inlet and outlet control valves. However, despite their moderate efficiency, challenges related to lubrication and sealing remain significant barriers to their development. Moreover, positive displacement expanders pose challenges due to their bulkiness, complexity, and numerous moving components, resulting in size and reliability issues for both domestic and commercial applications [20]. Additionally,

manufacturing costs rise significantly when building them on a small scale for domestic use due to the tight clearances between moving and stationary components, essential for minimizing leakage losses. Conversely, both impulse and reaction-type turboexpanders provide compactness due to their high rotational speed and fewer components. This attribute contributes to increased reliability compared to positive displacement expanders. Over the years, prominent HVAC manufacturers have introduced two-phase turboexpanders with moderate efficiencies as a straightforward and cost-effective solution for large-capacity commercial chillers, aiming to mitigate the most significant irreversibility in refrigeration cycles [21]. However, designing a turboexpander with acceptable efficiency poses more challenges in domestic applications, primarily due to the growing significance of losses in the context of lower available power.

In particular, impulse expanders, characterized by pressure drop occurring solely inside the nozzle, have demonstrated greater suitability for low mass flow rates and two-phase conditions. This is attributed to their optimal impeller speed and the absence of close running clearances [13]. Nevertheless, to the best of the authors' knowledge, two-phase impulse expanders tailored for CO_2 domestic heat pump applications have not yet been commercialized, calling for significant potential for their development and maturation. Tøndell [22] explored this avenue by developing and testing a radial outflow impulse expander for domestic CO_2 air-conditioning cycles. Unfortunately, the turbine faced challenges in reaching the intended speed due to excessive exit losses from the radial outflow design. To address this, the proposed solution involved adopting a radial inflow architecture to mitigate both exit and frictional losses. Further observations revealed that only 70% of the jet impacted the turbine blades, supported by flow visualization of the nozzle jet. This observation led the author to attribute the conical jet to incomplete refrigerant expansion inside the nozzle, resulting in an approximate nozzle efficiency of 60%. Tøndell also attempted to empirically assess the improved design by assuming a high nozzle efficiency of 85%. Despite this, due to significant windage and disk friction losses, he estimated the expander efficiency to be 39%. In a related effort, He et al. [13] analytically designed a Pelton-like turbine for a domestic refrigeration cycle working with R410a. Despite applying the Henry and Fauske model [23], for nozzle design, the tested turbine exhibited a maximum isentropic efficiency of only 32.8%. On the other hand, Hays and Brasz [24] analytically assessed the performance of a transcritical axial impulse turbine for recovering throttling loss in a small-scale CO_2 heat pump cycle. They estimated a very high turbine efficiency of 69%, the highest reported in the literature.

The significant discrepancy in the efficiency results of two-phase turbines highlights a lack of consensus in this field of research, emphasizing the necessity for further studies to obtain more reliable estimates of two-phase expander efficiency. Experimental results [13,22], which are generally more reliable, often indicate low efficiency for two-phase expanders in domestic heat pump cycles. This is attributed to the absence of design guidelines and the challenges posed by complex two-phase flow, small size, and high rotational speed of these expanders. These challenges underscore the ongoing need for advancements in the development of efficient two-phase impulse expanders for CO_2 heat pump applications. A critical aspect of this advancement lies in focusing on the design of an efficient nozzle capable of accommodating two-phase conditions.

High-fidelity shape optimization through computational fluid dynamics (CFD) has traditionally been prevalent in aerodynamics applications [25–27]. However, in recent years, CFD-based shape optimization has also been applied to ejector and nozzle design. For instance, Palacz et al. [28] used a genetic algorithm coupled with a two-phase homogeneous equilibrium CFD tool to optimize the shape of four different CO_2 ejectors designed for supermarket applications. The optimization results demonstrated a 6% increase in efficiency, smoother expansion along the motive nozzle, lower turbulence intensity inside the mixing chamber, and a more uniform velocity profile in the mixing section. Similarly, Lee et al. [29] used a two-phase non-equilibrium homogeneous CFD tool to optimize the shape of a two-phase R600a ejector. They employed a multi-objective genetic algorithm coupled with an online approximation-assisted optimization approach to maximize the ejector pressure lift and entrainment ratio. The optimization successfully identified a Pareto set for pressure lift and entrainment ratio with respect to the baseline geometry.

Ensuring efficient operations of a two-phase impulse expander intended for domestic CO_2 heat pumps heavily rely on an appropriate nozzle design. Since flow expansion and phase change occur entirely through the nozzle, a non-optimal nozzle design will significantly penalize the two-phase CO_2 impulse expander. Sub-optimal nozzle design generates shock waves inside or downstream of the nozzle, degrading performance and preventing a uniform jet from reaching the expander blades, thereby severely impacting rotor performance. Consequently, the resulting low-efficiency impulse expander cannot recover much of the power made available by replacing the lamination valve, leading to only a marginal COP gain, which may not justify the addition of the expander.

Experimental studies on nozzle design for impulse expanders [13,22] indicate that classical design strategies fail to achieve acceptable isentropic efficiency, primarily due to nozzle losses. Traditional design methods, such as the method of characteristics (MoCs) used for supersonic nozzles, are not applicable to CO_2 two-phase nozzles due to the discontinuity of the sound speed resulting from the phase change. To overcome this issue, we propose a design approach based on shape optimization combined with high-fidelity CFD simulations.

All shape optimization practices found in the literature regarding flashing flows inside nozzles focus on ejectors [28,29], where the main goal is to enhance mass entrainment and pressure lift by improving the mixing process within the ejector. In this study, we apply a shape optimization method to the nozzle of a Pelton turbine, with a primary focus on enhancing jet uniformity downstream of the nozzle in multiple operating conditions. This uniform jet ensures both optimal nozzle performance and improved Pelton wheel performance. Our detailed analysis of the impulse expander integrates a CFD assessment of the nozzle with a mean-line model for estimating Pelton wheel efficiency. Additionally, the entire computational framework for the turbine performance assessment is integrated with the system analysis to explore realistic off-design conditions, representing a significant advancement in the field of transcritical CO_2 heat pumps using expanders for energy recovery.

This paper follows a structured framework as outlined below. Initially, we introduce the CFD method for modeling two-phase flows. Subsequently, we present the shape optimization methodology, where we detail the surrogate-based optimization techniques and the formulation of the optimization problem. In Section 4, we apply the shape optimization approach to the nozzle designed for operation at cycle design conditions, presenting the outcomes of the optimization process. Moving to Section 5, we present the ASHP cycle, detailing its components, and describing the off-design control strategy. Section 6 focuses on the nozzle optimized for various operating conditions, including both design and off-design scenarios. We compare its impact on cycle performance with the baseline nozzle and the nozzle optimized solely for operation at design conditions, as presented in Section 4. Finally, in Section 7, we draw comprehensive conclusions based on our findings.

2. CFD Methods

The flow solver is a steady pressure-based homogeneous equilibrium method (HEM) implemented in ANSYS-Fluent®. HEM recovers the Favre-averaged Navier Stokes equations complemented with thermodynamic properties of the mixture at thermodynamic equilibrium. It employs an enthalpy-based energy equation instead of the standard energy equation expressed in terms of total enthalpy. This substitution is necessary to circumvent the ANSYS-Fluent® requirement of using

temperature as a state variable when non-ideal equations of state are adopted. With this modification, pressure and specific enthalpy can serve as independent state variables, facilitating the retrieval of thermodynamic equilibrium properties for the two-phase mixture according to a state-of-the-art equation of state [30]. Turbulence effects are modeled using the k-ω SST turbulence model, ensuring the boundary layer at the walls is well-resolved (maximum y^+ value of 3). Further details on the computational domain are provided in Section 4.2, which also covers the associated boundary conditions. More comprehensive information about the flow model and its implementation can be found in [31].

To speed up the calculation, a look-up-table (LUT) approach is implemented to access thermodynamic properties during flow solver iterations. LUT boundaries are defined to prevent extrapolation and are set as follows: $P \in [6, 140]$ bar and $h \in [90.7, 523.4]$ kJ kg^{-1}, with $h_{ref} =$ 200 kJ kg^{-1} at $T = 0\ ^{\circ}$C and saturated liquid condition. A grid of 660 $\times$ 1150 points is identified with uniform steps in pressure (0.20 bar) and specific enthalpy (0.38 kJ kg^{-1}). The LUT resolution is set following Romei et al. [31].

The system of equations (continuity, momentum, turbulent kinetic energy, turbulence dissipation rate, and energy) is solved sequentially: continuity and momentum equations are solved concurrently, followed by the two equations of the k-ω SST turbulence model, and finally, the enthalpy-based energy equation. Thermo-physical properties are updated subsequently through the LUT approach previously introduced. Advective terms of continuity, momentum, turbulence equations, and the enthalpy-based energy equation are discretized using the second-order upwind scheme, with a cell-to-cell flux limiter applied to minimize spurious oscillations near discontinuities. All diffusive terms employ a second-order central differencing scheme, with gradients computed via the least squares cell-based method. A second-order accurate method is selected for interpolating pressure from cell centers to cell faces.

The computational setup was validated in a prior study [31] against experiments conducted by Nakagawa et al. [32], which involved flashing flows of carbon dioxide under thermodynamic conditions similar to those of the present work. The predictions for pressure and temperature along the nozzle axis of the present computational method closely matched experimental data from pressure transducers and thermocouples, with maximum relative errors of 6.4% for pressure and 1.1% for temperature. Based on this validation, the assumption of thermodynamic equilibrium and homogenous flow is deemed appropriate for the aerodynamic modeling of the subsequent impulse-stage nozzles.

3. Shape optimization method

3.1. Surrogate interpolation

Shape optimization practices require a considerable number of evaluations of the objective functions, which may be prohibitive if such evaluation involves computationally expansive simulations, like those based on CFD. To mitigate this issue, a surrogate metamodel is utilized to approximate the objective function. Kriging [33] is an interpolation method based on a Gaussian process regression widely employed in surrogate-based optimization of noise-free datasets [34,35], chosen for its capacity to accurately capture the complexity of response functions in intricate optimization problems [26]. Among the various types of Kriging, this paper implements Ordinary Kriging, the most widely used method for approximating computational models. In Ordinary Kriging, the output of the computational model is approximated through a Gaussian process composed of a constant trend and a covariance function. This latter is implemented as Matérn 3/2 function [36]. One of the main advantages of Kriging modeling is that it returns both the predicted value $\widehat{y}$ and the prediction uncertainty $\widehat{s}$ for any value of the input variable $\boldsymbol{x}$.

In surrogate-based shape optimization, the metamodel is initiated by interpolating a dataset composed of evaluations of various geometric configurations obtained through CFD. Once the Kriging surrogate is constructed, the global optimum can be searched over the model. However, this procedure can easily lead to the optimization process falling into a local optimum, as the initial interpolation may not be sufficiently accurate to reveal the true optimum. For a robust search for the global optimum, the surrogate model accuracy can be improved by adding new points in the design space, in addition to the initial sampling points. In this study, the expected improvement (EI) [37,38] is used as an infill criterion to balance global exploration and local exploitation of the objective function, leveraging the information about the model uncertainty. The EI can be calculated as

$$\mathbb{E}[I(\boldsymbol{x})] = \begin{cases} (y_{min} - \widehat{y}(\boldsymbol{x}))\Phi\left(\frac{y_{min} - \widehat{y}(\boldsymbol{x})}{\widehat{s}(\boldsymbol{x})}\right) + \widehat{s}(\boldsymbol{x})\phi\left(\frac{y_{min} - \widehat{y}(\boldsymbol{x})}{\widehat{s}(\boldsymbol{x})}\right) & \widehat{s}(\boldsymbol{x}) > 0 \\ 0 & \widehat{s}(\boldsymbol{x}) = 0 \end{cases}, \tag{1}$$

where Φ and ϕ are the cumulative distribution function and the probability density function, respectively, and y_{min} is the best value of the objective function among the geometric configurations evaluated through the CFD.

The infill point can be determined by maximizing the function in Eq. (1) with a gradient-free global optimizer. In this study, differential evolution (DE) [39] from the Scipy library [40] is employed to find the infill point. Fig. 1 illustrates the evolution of the Kriging surrogate for the objective function initially constructed with four function observations. In each iteration, a new point corresponding to the maximum of the EI function is added to the set of sampling points. Subsequently, the objective function is evaluated at the added point using the high-fidelity computational model, and the surrogate representation is updated.

In optimization problems with constraints, it is crucial to locate the optimum within the feasible region of the design space, where the optimization constraints are satisfied. Let us consider a constraint $g(\boldsymbol{x}) < g_{max}$, and assume we have constructed a separate Kriging surrogate for the constraint function, denoted as $g(\boldsymbol{x})$. The probability that the constraint is fulfilled can be expressed as [41]

$$\mathbb{P}[g(\boldsymbol{x}) < g_{max}] = \Phi\left(\frac{g_{max} - \widehat{g}(\boldsymbol{x})}{s_g(\boldsymbol{x})}\right). \tag{2}$$

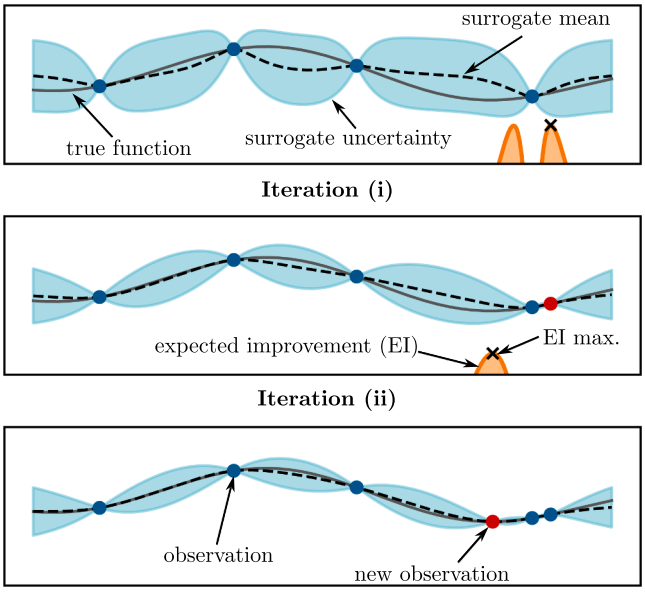

Fig. 1. Illustration of the expected improvement infilling criterion.

Here, $\hat{g}(\boldsymbol{x})$ and $s_g(\boldsymbol{x})$ represent the predicted value and the standard deviation of the prediction through the Kriging surrogate for the constraint function, respectively. Subsequently, the constrained EI can be defined as

$$\mathbb{E}_c[I(\boldsymbol{x})] = \mathbb{E}[I(\boldsymbol{x}) \cap g(\boldsymbol{x}) < g_{max}] = \mathbb{E}[I(\boldsymbol{x})] \cdot \mathbb{P}[g(\boldsymbol{x}) < g_{max}]. \tag{3}$$

3.2. Optimization problem

The generation of shock waves downstream of the nozzle can significantly deteriorate the performance of a two-phase impulse expander. If the nozzle geometry is not designed to accommodate the required expansion imposed by boundary conditions, the flow leaves the nozzle in either an over-expanded or under-expanded condition. In either condition, a series of expansion waves and oblique shock waves will appear downstream of the nozzle, causing local expansion and contraction in the jet boundary [42]. This local expansion and contraction of the jet will hinder a uniform jet from reaching the Pelton buckets. If the jet impacts the bucket in a region where the jet cross-section is expanded, a part of the conical jet may fail to impact the turbine blades effectively. Additionally, the severe interaction between shock waves and the jet results in liquid droplet scattering around the rotor, leading to increased windage loss [22]. Moreover, the interaction between shocks and the rotor can cause severe damage, reducing the rotor's useful life. Therefore, this study aims to optimize the nozzle for a series of operating conditions, including those occurring during off-design heat pump operations. Since the presence of shock waves introduces irreversibility, expressed in the form of entropy generation [43], the optimization objective is to minimize entropy generation within the operating envelope of the two-phase expander. The objective function of the optimization is defined as

$$F_{obj} = \sum_{i=1}^{op} \frac{s_{ax,i} - s_{in,i}}{s\left(p_{out,i}, h^t_{in,i}\right) - s_{in,i}}, \tag{4}$$

where s_{ax} represents the entropy evaluated at the nozzle axis at a specific downstream distance, and op denotes the number of operating conditions. Entropy generation due to shocks exhibits cumulative behavior; thus, the entropy evaluation point is situated far downstream of the nozzle outlet to capture the overall effect of shock waves before the flow mixes out. Based on the observation of the flow field, evaluating entropy at $z/L = 1.8$ is considered a good compromise, where z is axial distance and L is the nozzle length, capturing the overall effects of shocks while avoiding the consideration of mixing losses. It is crucial to note that entropy is solely evaluated on the nozzle axis to focus on capturing losses associated with shock waves. Any form of mass-weighted or area-weighted averaging would introduce contributions from the radial distribution of entropy, which includes losses associated with flow shear.

The denominator of Eq. (4) represents the overall entropy generation in each operating condition when the flow is brought to stagnation adiabatically at the corresponding outlet pressure. This normalization ensures that the entropy generation values are comparable across all operating conditions.

At each operating condition, the optimized nozzle design must be capable of providing the required refrigerant mass flow rate for the heat pump cycle. To ensure this, a constraint function is introduced to minimize the deviation of the nozzle mass flow rate, $\dot{m}$, from its reference value, $\dot{m}_{ref}$, at each operating condition. The Weighted Mean Absolute Percentage Error (WMAPE) is employed as a metric to represent the overall mass flow rate deviation for different operating conditions. It is defined as

$$WMAPE_{mass} = \sum_{i=1}^{op} \frac{\left|\dot{m}_i - \dot{m}_{ref,i}\right|}{\dot{m}_{ref,i}} .100, \tag{5}$$

where the mass flow rate is evaluated at the nozzle outlet section to exclude possible mass entrainment downstream of the nozzle exit. Given that the heating power of the heat pump is directly proportional to the refrigerant mass flow rate, a precision control criterion is set. A $WMAPE_{mass} < 3\%$ is chosen to restrict the mass flow rate deviation.

4. Single-point optimization

While the primary objective of this paper is to introduce a shape optimization tool capable of generating an optimized nozzle shape robust enough to deliver high performance under both design and off-design conditions of the heat pump cycle, this section exclusively concentrates on shape optimization at the design condition. This deliberate focus allows us to validate the shape optimization procedure, showcasing its capabilities initially in a simpler scenario before extending its application to the complete context involving design and off-design operating points.

4.1. Shape and parameterization

In shape optimization problems, a common approach involves parametrizing the geometry and introducing a limited number of control points (CPs) to modify the geometry by adjusting their positions. The placement of these CPs and their allowable range of variation define the design space for the optimization problem. It is crucial to restrict the movement of CPs to prevent the generation of irrelevant shapes.

To initiate the shape modification, a baseline nozzle geometry must be defined. The inlet section of the nozzle is designed based on a reference mass flow rate, assuming a relatively low Mach number of 0.05 at the inlet section. Both experimental [44] and numerical simulation [45] results confirm that in flashing flows of refrigerant inside a converging–diverging nozzle, the onset of two-phase flow occurs near the nozzle throat. Given the significant drop in the homogeneous equilibrium speed of sound for CO_2 at the onset of the two-phase flow, it is reasonable to assume a choked condition at the nozzle throat. Therefore, the geometric throat can be identified by maximizing the product of density and velocity.

For designing the diverging section of supersonic nozzles while working with an ideal gas, the MoCs have been commonly employed [46]. To initiate the MoCs for designing the diverging nozzle section, it is necessary to define the sonic line. However, since the speed of sound exhibits a discrete drop at the onset of phase change, defining the sonic line becomes challenging. Therefore, following the approach used by Tøndell [22], a linear diverging section with a constant divergence angle (1.5°) and a length equal to 10 times the throat diameter is employed.

By knowing the cross-section of the nozzle at the inlet and throat, as well as the shape of the diverging section, the baseline nozzle geometry is constructed using a B-spline [47] curve, which is a common method for designing aerodynamic profiles. The baseline nozzle geometry and its corresponding geometrical parameter values are illustrated in Fig. 2 and summarized in Table 1, respectively.

For controlling geometrical variations in the nozzle, one passive and five active CPs are introduced, as depicted in Fig. 2. Additionally, two parameters, L_{conv} and L_{div}, govern the lengths of the converging and diverging sections of the nozzle, respectively. The passive CP, denoted as

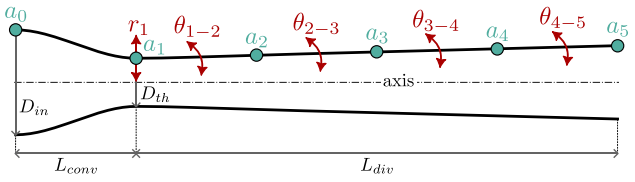

Fig. 2. Nozzle geometrical parameters and parameterization for the shape optimization.

Table 1
Geometrical parameter values for baseline geometry.

Parameters	Values	Units
D_{in}^{base}	1.8	mm
L_{conv}^{base}	2.1	mm
D_{th}^{base}	0.8	mm
θ_{i-j}^{base}	1.5	deg
L_{div}^{base}	8.2	mm

a_0, remains fixed at the nozzle inlet to maintain a constant inlet diameter and enforce a zero slope at the entrance. At the nozzle throat, the first active CP (a_1) is positioned to control the dimensions of the nozzle throat through vertical displacement, while maintaining a zero-slope constraint at the throat. Distributed evenly along the diverging section, the remaining active CPs (a_{2-5}) play a crucial role. By adjusting the angles of their connecting lines relative to the horizontal axis, piecewise control over the diverging angle in the nozzle diverging section is achieved. Similar to the baseline geometry, a B-spline curve smoothly connects all the CPs.

It is important to note that a control algorithm is implemented to restrict the displacement of CPs, thereby preventing local reductions in the nozzle cross-section in the diverging section. The decision to place most CPs in the diverging section is based on the understanding that this section deals with two-phase flow and unconventional gas dynamics, whereas the converging section primarily handles single-phase flow, where changes to its shape are less critical to the nozzle's performance. However, the validity of this assumption will be assessed in the upcoming sections.

To determine the permissible range of variation for each geometric design variable, we establish the design space within which the nozzle geometry is allowed to evolve. The chosen range for each geometrical parameter, as illustrated in Fig. 2, is detailed in Table 2. The bounds of these parameters must be carefully selected to strike a balance between covering a broad range of geometrical variations and ensuring that the nozzle shape remains within acceptable limits for the flow solver to converge to a solution. For instance, excessively large diverging angles may lead to the formation of strong shock waves, potentially causing the CFD solution to fail to converge.

4.2. Computational domain and grid selection

The computational domain, along with its dimensions for the baseline geometry, is illustrated in Fig. 3. Axisymmetry is exploited by including only half of the geometry in the computational domain. A large plenum is integrated into the nozzle discharge to make possible flow evaluation downstream of the nozzle, where the Pelton expander will be placed. Additionally, adding a plenum is essential for capturing potential normal and oblique shocks, as well as expansion fans that may occur downstream of the nozzle outlet when the nozzle geometry is not tailored to the boundary conditions.

The design operating conditions of the nozzle, based on the typical working conditions of the expansion valve in domestic CO_2 heat pumps for water heating [48–50], are summarized in Table 3. It is important to note that the expansion begins from a single-phase and extends into the saturation dome. Assuming an isentropic expansion, the vapor quality at the nozzle outlet would be 0.23.

Table 2
Geometrical design variables with their bounds.

Geometrical Parameter	Lower bound	Upper bound
L_{conv}	L_{conv}^{base}	$1.2L_{conv}^{base}$
L_{div}	$0.5L_{div}^{base}$	$1.5L_{div}^{base}$
r_1	$0.4D_{th}^{base}$	$0.6D_{th}^{base}$
θ_{i-j}	0.3 (deg)	3.0 (deg)

Total pressure and total enthalpy are prescribed at the inlet section based on the values detailed in Table 3. For turbulent boundary conditions, a turbulent intensity of 1% and a turbulent viscosity ratio of 1 are assigned, representing the low turbulence levels typical in nozzle expanding flows from a reservoir. ANSYS-Fluent® utilizes these inputs to determine the corresponding values of k and ω at the inlet using its built-in algorithms. At the plenum outlet, static pressure is specified along with a zero-gradient condition for static enthalpy, the latter needed for the enthalpy-based energy equation. Adiabatic and no-slip conditions are selected for the walls of the computational domain. It is worth mentioning that the upper and left walls of the plenum can also be modelled as outlets. However, this approach may challenge the simulation convergence due to significant backflow caused by flow recirculation at the boundaries. To mitigate this issue, larger plenum dimensions may be necessary, albeit at the cost of increased computational resources, particularly for optimization problems requiring numerous flow simulations.

A grid convergence assessment is initially conducted by generating three hexahedral grids with an increasing number of elements. As the mesh resolution increases, the number of elements is doubled in each step in the axial direction across the entire domain. Meanwhile, in the radial direction, the number of elements is doubled only in the plenum region to ensure consistent wall resolution on the nozzle wall. To address turbulence near the nozzle wall, a first-layer wall distance of 6.1×10^{-8} m with a smooth expansion ratio of 1.1 is selected, ensuring at least 3 cells inside the viscous sub-layer and maintaining a maximum y^+ value of less than 3 along the entire length of the nozzle wall. At the nozzle throat, a mesh resolution of 6.1×10^{-7} m is achieved for the medium mesh. The coarse grid (grid 1) comprises 26136 elements, while the medium (grid 2) and fine (grid 3) grids consist of 51703 and 118496 elements, respectively. The results of the grid convergence study, in terms of main flow variables, are quantified by computing the grid convergence index (GCI) using the Richardson extrapolation method [51,52].

Knowing the values of key variables $\psi^{(i)}$ obtained by three meshes (with $i = 1, 2, 3$ referring to the corresponding computational grid), the apparent order $\mathscr{P}$ of the method, the extrapolated value ψ_{ext}, the approximated e_a and extrapolated e_{ext} relative errors, and the GCI can be evaluated [53]. The key variables are entropy on the nozzle axis at the evaluation point ($z/L = 1.8$) and mass flow rate at the nozzle outlet, as the former is crucial for the objective function, and the latter is crucial for the constraint function of the optimization problem.

All the results from this grid assessment are comprehensively presented in Table 4, encompassing the GCI for the medium-grid solution. The maximum GCI is identified for the mass flow rate, totaling 0.35%, while a notably smaller error impacts the entropy estimate, specifically 0.04%. The fine-grid GCI obviously reduces compared to its medium-grid counterpart, being 0.13% for mass flow rate and less than 0.01% for entropy. In addition to the discretization error, computational cost is a pivotal factor in decision-making. Given the intention to conduct multi-point optimization in the subsequent sections and observing the relatively low GCI for both mass flow rate and entropy in the medium grid, this latter grid is chosen for further assessments in this paper. This selection aims to mitigate computational costs without significantly compromising accuracy. It is crucial to note that as the optimization progresses and the nozzle geometry becomes more refined, potentially alleviating strong shocks, the discretization errors are expected to further diminish compared to those reported for the baseline nozzle geometry.

4.3. Convergence verification

To ensure the reliability of the surrogate models for optimization purposes, their accuracy is validated against high-fidelity function evaluations, specifically using CFD. Two surrogate models—one for the

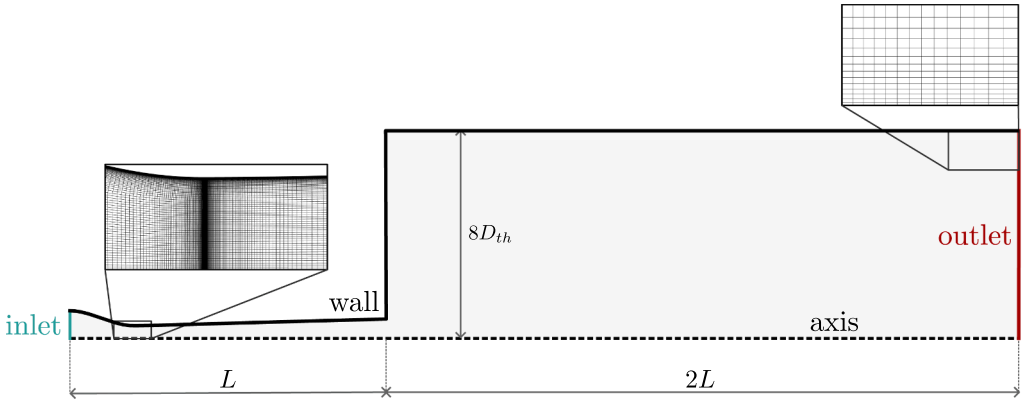

Fig. 3. Computational domain dimensions depicting the baseline geometry, utilizing a medium computational mesh, and featuring specified boundary conditions.

Table 3
Operating conditions of the nozzle at the design point.

Parameters	Values	Units
P^t_{in}	94.2	bar
T^t_{in}	27.7	°C
P_{out}	37.7	bar
$\dot{m}_{in}$	38.0	g s^{-1}

Table 4
Grid analysis outcomes.

ψ =	$\dot{m}$	s_{ax}
$\psi^{(1)}$	37.57 (g s^{-1})	1214.9 (J kg^{-1} K^{-1})
$\psi^{(2)}$	37.36 (g s^{-1})	1219.1 (J kg^{-1} K^{-1})
$\psi^{(3)}$	37.30 (g s^{-1})	1219.4 (J kg^{-1} K^{-1})
$\mathscr{P}$	2.45	5.48
ψ_{ext}	37.26 (g s^{-1})	1219.5 (J kg^{-1} K^{-1})
e_a	0.18%	0.03%
e_{ext}	0.28%	0.03%
GCI	0.35%	0.04%

objective function and one for the constraint function—are constructed based on different numbers of initial design samples obtained through the Latin hypercube sampling (LHS) technique [54]. These surrogate models are then validated against 50 test data points generated using a different LHS sample pool and assessed using the CFD model. The global accuracy of the surrogate models is quantified using the normalized root mean squared error (NRMSE) [26], defined as

$$NRMSE = \frac{\sqrt{\sum_{i=1}^{N_{test}} \left(y^i_{test} - \widehat{y}^i_{test}\right)^2 / N_{test}}}{\left(y_{max} - y_{min}\right)_I}, \tag{6}$$

where y^i_{test} and $\widehat{y}^i_{test}$ represent the response evaluated by CFD and the surrogate model prediction at the i^{th} test sample, respectively. The response value y is either the objective function or constraint function value for their respective error estimations. N_{test} is the number of testing data samples and $\left(y_{max} - y_{min}\right)_I$ represents the difference between the maximum and minimum response values in the initial sample data set.

The variation of NRMSE with the size of the initial design sample is depicted in Fig. 4. Notably, the surrogate model for the constraint function closely tracks the CFD values, even when constructed using a relatively small initial sample dataset. However, the surrogate model for the objective function requires a larger initial design sample dataset to achieve acceptable prediction accuracy. In this study, an initial design sample dataset comprising 50 samples is chosen to construct the initial

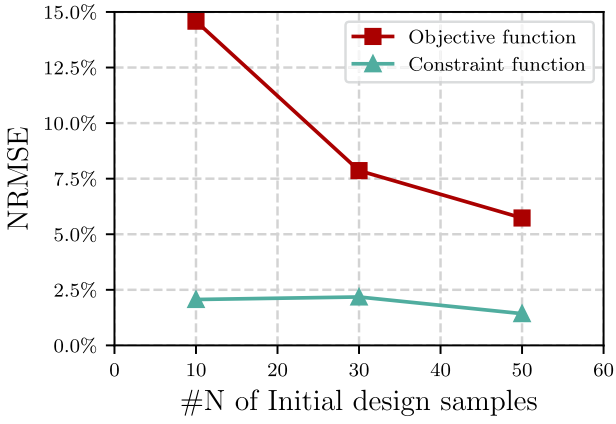

Fig. 4. Accuracy of the objective and constraint surrogate models against CFD results after the initial training.

surrogate models. This selection yields good prediction accuracy for both the objective function and constraint function surrogates, with NRMSE values of 5.7% and 1.4%, respectively. Further increasing the initial sample dataset size appears to only marginally enhance the surrogate accuracy.

A fixed budget of 25 infill points is utilized to enhance the accuracy of the surrogates, with sequential updates based on the constrained EI infill criteria. The convergence history of both the objective and constraint functions is comprehensively presented in Fig. 5. Upon analyzing the convergence history, it becomes evident that the uncertainty of the initial surrogate predictions, constructed from the initial design samples (its extent depicted by the vertical dashed line in Fig. 5), is relatively low. This is attributed to the infilling points being strategically added at the minima of both the objective and constraint functions. The incorporation of 25 additional design samples appears to be sufficient, as the values of the objective and constraint functions converge towards their global minimum. Further additions are expected to have minimal impact on the values of both functions. It is worth mentioning that the constraint function has successfully ensured that the mass flow rate deviation from its reference design value remains within the maximum allowable limit ($WMAPE_{mass} < 3\%$).

However, further validation of the shape optimization process is necessary regarding the geometrical variation of the nozzle. Fig. 6 depicts the L_2-norm magnitude of the CP coordinates for consecutive optimal shapes, including all CPs and specifically those located along the diverging section of the nozzle (a_j where $j \in [1, 2, \cdots, 5]$). The L_2-norm magnitude is calculated as

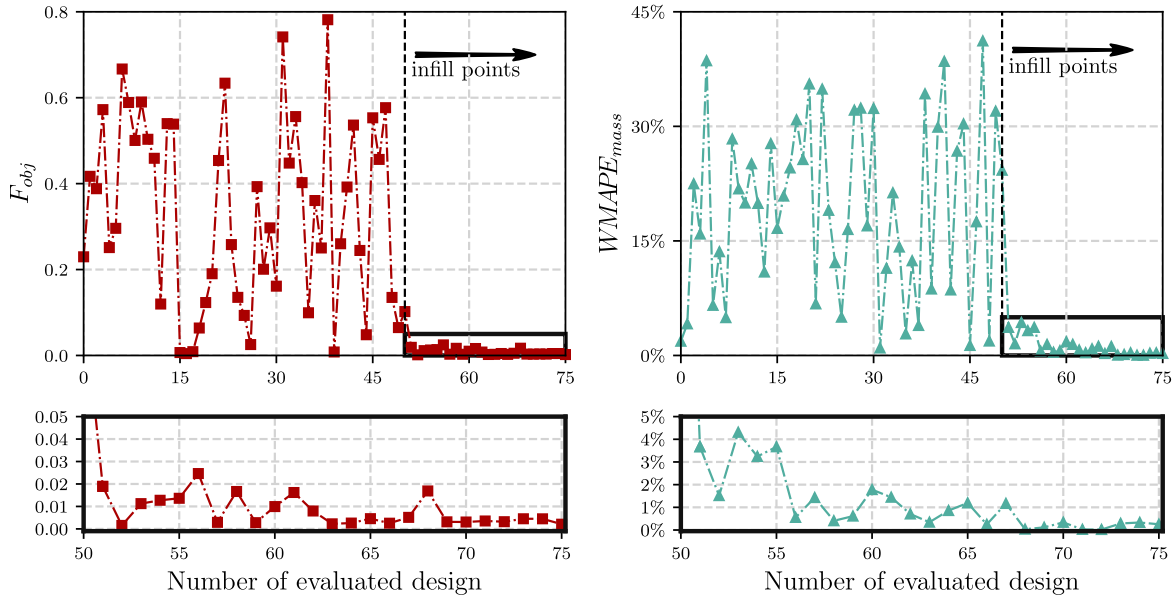

Fig. 5. Convergence history of the objective function (left) and the constraint function (right). Detailed convergence of both functions, following the addition of points based on infilling criteria, is illustrated at the bottom.

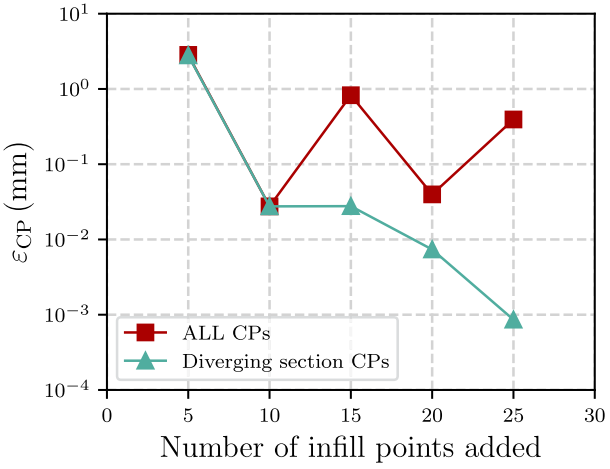

Fig. 6. Change in coordinates of the CPs for two consecutive optimum nozzle shapes, each evaluated after the addition of 5 infill points.

$$\varepsilon_{CP} = \sqrt{\sum_{j}^{N_{CP}} \left[\left(z^{i}_{CP\,j} - z^{i-1}_{CP\,j} \right)^2 + \left(r^{i}_{CP\,j} - r^{i-1}_{CP\,j} \right)^2 \right]}, \tag{7}$$

where z_{CP} and r_{CP} are the axial and radial coordinates of the CPs, respectively, and N_{CP} is the number of CPs considered for the calculating the L_2-norm magnitude. The indices i and $i-1$ correspond to the optimized shapes updated after adding a certain number of infill points and the previous optimized shape, respectively, with a step of 5 infill points between consecutive optima. For instance, the L_2-norm magnitude after adding 15 infill points measures the difference between the optimal shapes with 15 and 10 additional samples. While the L_2-norm of all CPs between two consecutive optimal designs exhibits an oscillatory trend, the L_2-norm excluding the CP in the converging section (a_0) converges to a minimum. This indicates that the shape of the diverging section of the nozzle remains relatively stable as the optimization progresses. This observation is consistent with expectations, as changes in the converging section, primarily affecting single-phase expansion, are anticipated to have negligible effects on shock losses. Therefore, the length of the converging section of the nozzle varies randomly within the allowable design space during optimization.

The optimization results must be independent of the initial design sample used for constructing the surrogate models, also known as the design of experiments (DoE) in the literature. Otherwise, the objective function is considered multi-modal and the optimization may be trapped in local optima. To verify this, 10 different sets of DoE are constructed based on LHS, and the final optimization results obtained from each set of DoE are compared, as presented in Fig. 7. As expected, the axial coordinate of the CP located at the converging section of the nozzle (a_0) exhibits the maximum variation compared to the other CPs, with a standard deviation (STD) of 0.69 mm. On the other hand, the coordinates of the CPs located at the diverging section of the nozzle (a_{1-5}) show negligible variation in both the axial (z) and radial (r) directions across different sets of DoE, with a maximum STD of 0.06 mm for a_5 and 0.01 mm for a_1 in the z and r directions, respectively.

The optimized nozzle entropy generation, normalized with the entropy generation of the baseline nozzle, is also presented for each optimized nozzle profile obtained by different sets of DoE in Fig. 7. All optimized nozzles have significantly reduced the entropy level at the axis, with an average reduction of 98.3% compared to the baseline nozzle geometry. Entropy generation from the inlet to the evaluation point decreased from 7.4 J kg^{-1} K^{-1} for the baseline nozzle to 0.1 J kg^{-1} K^{-1} on average for the 10 optimized nozzle profiles obtained from different sets of DoE. This reduction indicates that the optimization effectively eliminates irreversibilities caused by shock waves, achieving nearly isentropic expansion in the jet core. The small remaining entropy generation is due to near-isentropic pressure waves. This near-isentropic expansion is observed only in the jet core, while there is considerable entropy generation in the nozzle boundary layer and in the shear layer between the jet and the stationary fluid in the plenum due to velocity gradients. Moreover, all optimized nozzles satisfy the constraint on mass flow rate ($WMAPE_{mass} < 3\%$). The normalized entropy generation and $WMAPE_{mass}$ of the optimized nozzle geometries show STDs of 0.7% and 0.6%, respectively, indicating that the optimization outcomes using different DoEs are equivalent and the optimization outcome is

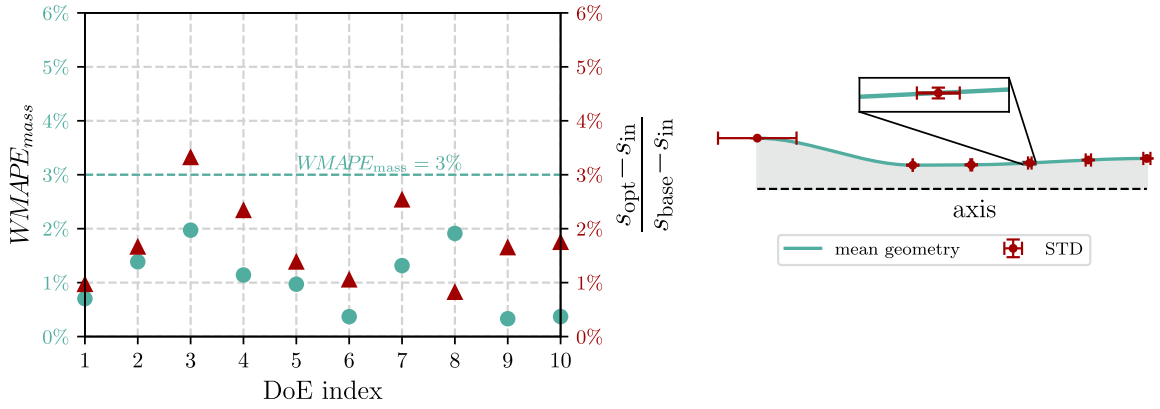

Fig. 7. Comparison of nozzle shape optimization results using 10 different sets of design of experiments (DoE). (left) Normalized entropy generation and WMAPE of mass flow rate for each optimized nozzle geometry obtained from different DoE sets, along with the allowable deviation of mass flow rate from the reference design value. (right) Mean nozzle shape with CPs mean positions and their standard deviation (STD).

independent of the DoE used for constructing the surrogate models.

4.4. Single-point optimization outcome

The shapes of the optimized and baseline nozzles are illustrated in Fig. 8. The most significant modification involves a 49.2% reduction in the length of the diverging section of the optimized nozzle compared to the baseline, accompanied by a 15.8% decrease in the nozzle outlet diameter. This alteration aims to prevent flow over-expansion. Apart from disparities in the converging sections, the throat dimensions of both nozzles are remarkably similar, with only a 0.9% increase in the optimized case. This similarity is because both nozzles are designed to deliver the same mass flow rate. Throat dimensions are crucial parameters that affect the mass flow rate through the throat under choked conditions, given the fixed inlet diameter and inlet boundary conditions.

In the near downstream of the nozzle throat, the optimized nozzle exhibits a smaller diverging angle, measuring 0.32° compared to the baseline value of 1.5°. This adjustment aims to ensure a smoother variation of the cross-section near the nozzle throat, where phase change occurs and the flow becomes supersonic due to the drop in sound speed in two-phase conditions. This smoother variation helps avoid abrupt changes in the flow direction, reducing the likelihood of local weak shock waves and expansion fans inside the nozzle.

The optimized nozzle demonstrates a limited increase in cross-section in the diverging section, resulting in a more gradual expansion of the flow compared to the baseline nozzle. This observation is supported by the pressure field contour shown in Fig. 9. In the baseline nozzle, over-expansion leads to the formation of strong shock waves near the nozzle outlet, resulting in a chain of shock waves and expansion fans downstream of the nozzle. The shape optimization successfully eliminates these strong shock waves, as depicted in the pressure field of the optimized nozzle (top half of Fig. 9).

The velocity fields of both the baseline and optimized nozzles are compared in Fig. 10. Over-expansion of the flow in the second half of the diverging section in the baseline nozzle leads to increased vapor generation inside the nozzle, causing high velocities near the nozzle outlet. In two-phase nozzles, vapor generation is considered a crucial factor in flow acceleration [55]. Reduced vapor generation in the diverging section of the optimized nozzle mitigates flow acceleration in the second half of the diverging section compared to the baseline. Furthermore, the velocity profile outside the optimized nozzle is more uniform due to the mitigation of shock waves through shape optimization. This uniform velocity profile can be advantageous when a Pelton wheel is installed, as it can significantly increase rotor life by reducing shock interactions with the buckets and minimizing losses associated with liquid droplet scattering around the wheel [22].

To quantify the gain of the optimization practice, nozzle efficiency is introduced as an evaluation metric. Nozzle efficiency is defined as

$$\eta_{noz} = \frac{\sum_{i=1}^{5} \frac{\dot{m}_{z_i}}{\dot{m}_{out}} \eta_{vel,z_i}}{5}. \tag{8}$$

The nozzle efficiency is averaged over five different axial distances downstream of the nozzle, denoted as $z_i \in [1.1L, 1.2L, \cdots, 1.5L]$. One reason for this averaging is that the Pelton wheel interacts with the flow at a range of axial coordinates downstream of the nozzle outlet. Additionally, averaging mitigates local effects introduced by shock waves and expansion fans. The objective is to establish a performance metric that reflects overall nozzle performance rather than being influenced by localized phenomena. For instance, evaluating efficiency at an axial location coinciding with a local expansion fan may result in higher efficiency due to increased velocity. Averaging over multiple locations provides a more representative measure, reducing the impact of localized variations.

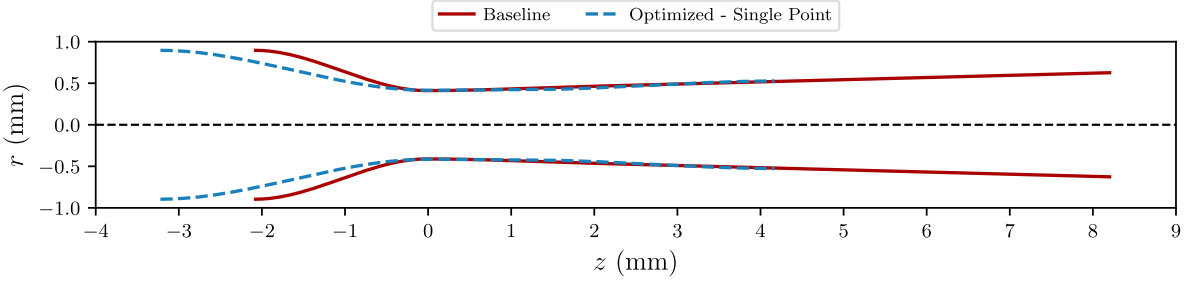

Fig. 8. Geometrical comparison of the optimized and baseline nozzles.

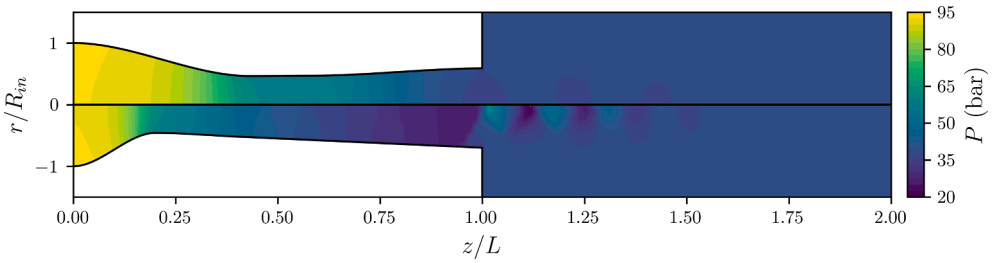

Fig. 9. Pressure field comparison between the optimized nozzle (top) and the baseline nozzle (bottom).

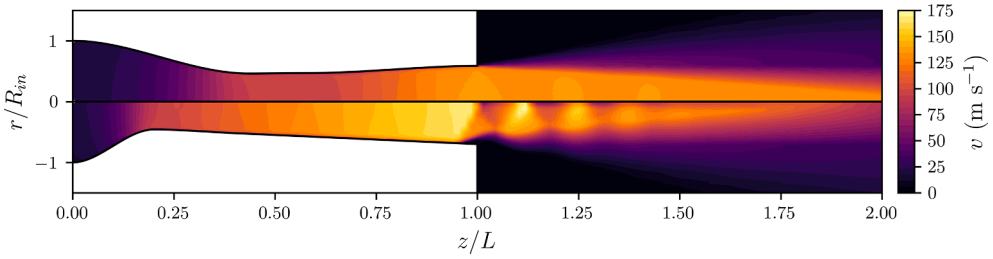

Fig. 10. Velocity field comparison between the optimized nozzle (top) and the baseline nozzle (bottom).

The term $\frac{\dot{m}_{\bar{S}_{z_i}}}{\dot{m}_{out}}$ represents the ratio of the mass flow rate passing through the evaluation surface $(\bar{S}_{z_i})$ to the mass flow rate measured at the nozzle outlet $\left(\dot{m}_{out}\right)$. As the nozzle discharges into a plenum filled with two-phase CO_2 at the static pressure assigned to the domain outlet, significant mass and momentum exchange occurs between the high-speed jet and the nearly stationary fluid inside the plenum. This exchange results in strong velocity gradients between the high-speed core of the jet and the stationary fluid, as depicted in the velocity field presented in Fig. 10. A portion of the jet kinetic energy is expended to accelerate the stationary fluid within the plenum. To account for this energy exchange, the mentioned mass ratio is defined within the efficiency calculation of the nozzle, drawing an analogy with the mass entrainment ratio in the definition of ejector efficiency. The expression

$$\eta_{vel,z_i} = \frac{\int \rho \left(V^2/V_{is}^2\right) \vec{V} \cdot \overrightarrow{dS}}{\int \rho \vec{V} \cdot \overrightarrow{dS}} \tag{9}$$

represents the mass-weighted average of the local isentropic efficiency (V^2/V_{is}^2) of the nozzle. This integral is calculated on the evaluation surface, considering the radial variation of nozzle efficiency. Following the principles of conventional Pelton turbine analysis, the evaluation surface is taken as the nozzle outlet area [56].

The nozzle efficiencies, calculated using Eq. (8), are presented in Table 5, alongside the mass flow rate deviation, which serves as the constraint imposed by the heat pump operating condition. Both the baseline and optimized nozzles meet the required mass flow rate criteria ($WMAPE_{mass} < 3\%$). The optimization process results in a notable improvement of 14.9% in nozzle efficiency compared to the baseline, indicating a significant enhancement. It is essential to note that in real-world scenarios, CO_2 liquid and vapor are expected to separate due to gravity, resulting in the presence of only vapor in the plenum where the nozzle discharges. With CO_2 vapor having lower density, reduced shear losses and corresponding higher efficiency can arguably be attained.

Table 5
Baseline and optimized nozzle performance.

Case	$\dot{m}$ (g s^{-1})	$\frac{\lvert\dot{m}-\dot{m}_{ref}\rvert}{\dot{m}_{ref}}.100$ (%)	η_{noz} (%)
Baseline	37.4	1.9	66.3
Optimized	37.9	0.3	76.2

5. System analysis

5.1. System assumptions and methodology

The main cycle process of the transcritical ASHP cycle for water heating, as depicted on the P-h diagram in Fig. 11, proceeds as follows: CO_2 vapor undergoes pressurization to reach the supercritical state in the compressor (1–2). Exiting the compressor, it releases heat to the water in the gas cooler (2–3), raising the water temperature from $T_{w,in}$ to $T_{w,out}$. Subsequently, CO_2 undergoes expansion to a lower temperature and pressure state facilitated by a Pelton expander, which recovers a

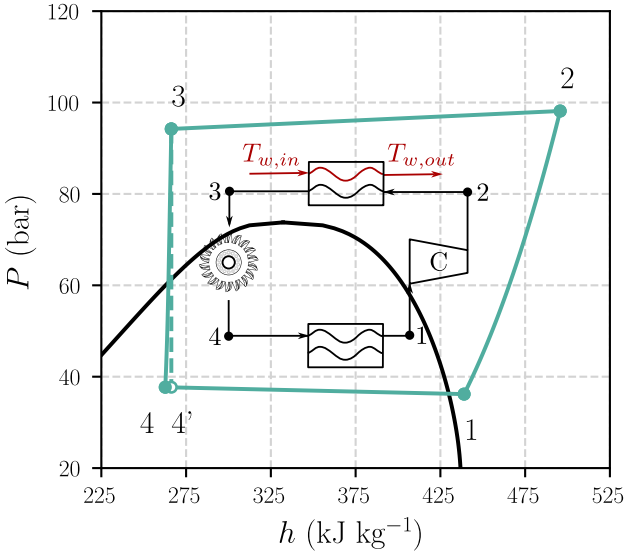

Fig. 11. Presentation of the heat pump cycle on a *P-h* diagram and the cycle configuration. The notation 4′ indicates the thermodynamic states achieved via an isenthalpic transformation (with a throttling valve replacing the Pelton turbine).

portion of the expansion energy (3–4). The isenthalpic expansion path (3–4′), typically observed in conventional expansion valves, is also represented by the dashed line. Finally, in the evaporator (4–1), the gas–liquid two-phase CO_2 absorbs heat from the air, completing the cycle.

In domestic heat pump applications, a simplified cycle configuration, akin to the one illustrated in Fig. 11, is commonly utilized. This approach helps manage and reduce the significant capital costs associated with the cycle, aligning with strategies identified in other studies on CO_2 heat pumps for domestic applications [49,50].

For the compressor, a two-stage volumetric compressor with a rolling piston, similar to the one used by Yang et al. [50], is assumed. The displacements for the 1st and 2nd stages are set at 4.5 cm^3 and 3.3 cm^3, respectively. By understanding the dependence of volumetric and isentropic efficiency on the pressure ratio across the compressor, the refrigerant mass-flow rate at specific compressor speed, along with the outlet states of the CO_2, can be calculated. A constant superheating of refrigerant (ΔT_{sh}) equal to 5°C is assumed at the evaporator outlet. Additionally, a pressure loss of 4% of the inlet pressure is considered on the refrigerant side of both the gas cooler and evaporator. The auxiliary power consumed by the evaporator fan and the water recirculating pump between the hot water user and the gas cooler is neglected.

A dedicated mean-line code has been developed to calculate the main dimensions and power output of the Pelton wheel, based on the mass-weighted average velocity and discharge mass flow rate of the jet exiting the nozzle. The code accounts for frictional losses between the refrigerant and the buckets, as well as windage loss due to the high-speed rotation of the wheel inside the CO_2 vapor at evaporator pressure [56]. Given that the density of CO_2 vapor at the evaporator pressure relevant to ASHP is approximately 100 times that of air density, and considering the high rotational speeds in these small-scale machines (in the order of 100000 rpm), windage loss is expected to be the dominant source of loss within this machine. A constant conversion efficiency of 90% is assumed for mechanical to electrical energy.

5.2. Identification of boundary conditions

According to Cabello et al. [48], the refrigerant outlet temperature from the gas cooler ($T_{gc,out}$) and the evaporation temperature (T_{eva}) are considered the most important cycle variables in transcritical CO_2 reverse cycles, influencing the COP of the cycle. The former depends on the water inlet ($T_{w,in}$) and outlet temperatures ($T_{w,out}$) from the gas cooler, while the latter is mainly a function of the ambient temperature (T_{amb}). It is common to set the water outlet temperature to a set point temperature of around 70°C, recognized as suitable for domestic applications in terms of legionella prevention [57]. Cui et al. [49] analyzed the effect of $T_{w,in}$ to the gas cooler and showed that both COP and heating capacity $\left(\dot{Q}_{gc}\right)$ reduced with an increase in $T_{w,in}$. Wang et al. [58] conducted an experimental analysis to evaluate the effect of T_{amb} on the performance of the heat pump cycle and found that the system performance decreases as T_{amb} decreases from 10°C to −10°C.

Cui et al. [49] proposed a control strategy to maintain a constant $\dot{Q}_{gc}$ by increasing the compressor rotational speed as $T_{w,in}$ increases or the evaporation temperature decreases due to the reduction in T_{amb}. They demonstrated that with this control strategy, $\dot{Q}_{gc}$ can be held approximately constant under designed conditions, with no degradation of the average COP. In this study, the same control strategy is implemented to keep $\dot{Q}_{gc}$ constant while maintaining $T_{w,out}$ at 70°C, even when $T_{w,in}$ and evaporation temperature change in off-design conditions. Determining the $T_{gc,out}$ and T_{eva} in off-design conditions requires detailed modeling of the heat exchangers, as reported in the work of Yang et al. [50]. However, in CO_2 heat pump studies, it is common to treat $T_{gc,out}$ and T_{eva} as independent variables and study the system performance at different levels of these parameters [48,59]. Similarly, this study explores two distinct levels of refrigerant temperature at the gas cooler outlet, specifically 27.7°C and 43.5°C. These values are chosen to depict variations in the return water temperature to the gas cooler $T_{w,in}$, reflecting diverse usage requirements on the heat user side. Additionally, two levels of T_{eva}, 3°C and −10°C, are considered to account for the impact of fluctuations in T_{amb} on the cycle performance. This variation is particularly relevant for ASHP, where the heat source temperature is prone to fluctuation.

The off-design condition of the system, considering the matching between the compressor and expander nozzle to maintain $\dot{Q}_{gc}$ constant at the designed value, is calculated by the algorithm presented in Fig. 12. As the nozzle operates under choked conditions, the mass flow rate of the nozzle depends solely on the inlet thermodynamic states, specifically total pressure and temperature. Nozzle maps are generated for the optimized nozzle shape obtained in Section 4.4, considering two different values of $T_{gc,out}$, for a range of inlet total pressures ranging from 80 bar to 140 bar. The variation of mass flow rate with inlet total pressure and total temperature is reported in Fig. 13. The nozzle mass flow rate at each inlet total temperature increases linearly with the rise of total inlet pressure. Thus, linear regression can be used to approximate the relation between nozzle mass flow rate and inlet total pressure without introducing a large error. It is noteworthy to mention that since the baseline and optimized nozzles have the same inlet dimensions, and the throat diameter of the optimized nozzle is only 0.9% larger than that of the baseline nozzle, under choked conditions, only the dimensions of the converging section can affect the mass flow rate. Therefore, it is expected that the same map remains valid for the baseline nozzle as well.

The off-design operating parameters, calculated using the algorithm

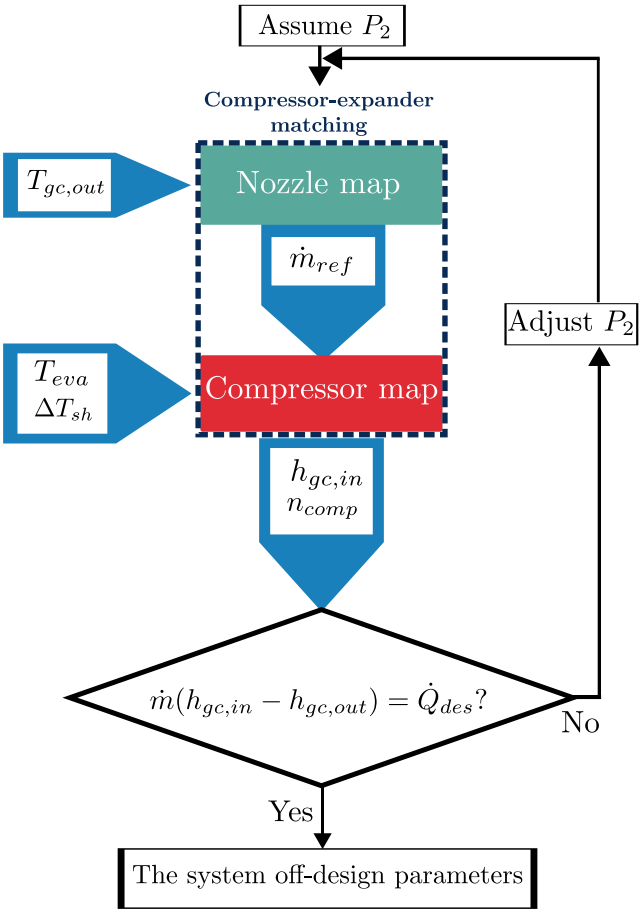

Fig. 12. Schematic diagram of system off-design calculation algorithm.

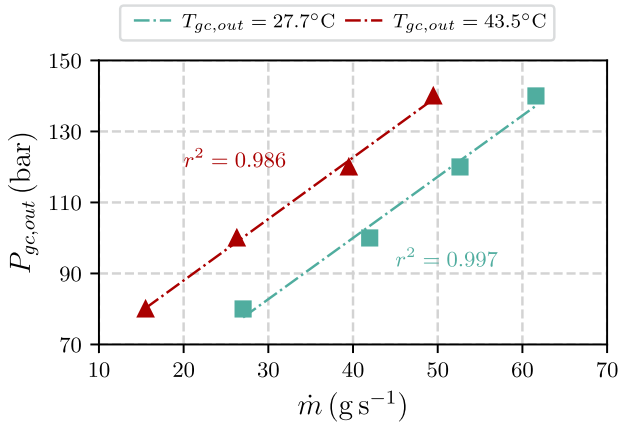

Fig. 13. Optimized nozzle operating map. Linear regression (dashed lines) and coefficient of determination (r^2) reported for each inlet total temperature.

illustrated in Fig. 12 and based on the nozzle map presented in Fig. 13, are summarized in Table 6 along with the design operating condition. Off-design A corresponds to operation under lower ambient temperatures than the design condition. Off-design B represents operation with an increased water return temperature to the gas cooler, resulting from lower heating demand on the user side. Off-design C considers both effects simultaneously.

6. Multi-point optimization

6.1. Multi-point optimization outcome

Given the substantial variation in nozzle boundary conditions during off-design operation, a nozzle optimized specifically for the design condition is not expected to maintain satisfactory performance in off-design conditions. Consequently, a multi-point optimization is conducted in this study to achieve satisfactory performance across the entire range of operating conditions. Similar geometrical parameterization to the single-point optimization task is applied to the baseline nozzle shape. The shapes of the baseline nozzle, the nozzle optimized for the design condition, and the nozzle optimized for multi-point operation are depicted in Fig. 14. Similar to the nozzle optimized for single-point operation, the length of the nozzle converging section is significantly reduced by 53.4% compared to the baseline nozzle, accompanied by an 11.0% reduction in the outlet diameter relative to the baseline nozzle. As a result of the mass flow rate constraint, the throat diameter of the multi-point optimized nozzle is remarkably similar to both the baseline and single-point optimized nozzles, with only a 0.5% larger throat diameter compared to the baseline.

Upon comparing the variation of the nozzle cross-section along the diverging section, it is evident that the multi-point optimized nozzle exhibits a larger cross-section increment along its diverging section length compared to the single-point optimized nozzle. This adaptation is designed to accommodate the larger expansion required when progressively moving from the design condition to off-design condition C. Nevertheless, the cross-section enlargement in the diverging section of the multi-point optimized nozzle remains limited compared to the baseline, ensuring optimal performance at the design operating condition.

To compare optimization results, Fig. 15 illustrates pressure variations along the axis of the computational domain for three nozzle shapes. Under the design condition, the single-point optimized nozzle achieves shock-free expansion, in contrast to the severe shock waves downstream of the baseline nozzle. The multi-point optimized nozzle displays relatively moderate shock waves in this scenario.

In off-design A, as the outlet boundary pressure decreases, the single-point optimized nozzle, tailored for the design condition, shows under-expansion, generating shock waves and expansion fans. The multi-point optimized nozzle experiences less under-expansion, while the baseline nozzle still over-expands the flow, resulting in slightly more severe shock waves compared to its multi-point optimized counterpart.

In off-design B, as the inlet state shifts towards the right of the saturation dome (from $s_{in}/s_{cr} = 0.85$ in the design condition to 0.93, where s_{cr} is the entropy of the critical point), the vapor mass fraction increases on the onset of two-phase flow, intensifying flow acceleration and causing more severe depressurization in the diverging section. However, despite the higher depressurization rate, the single-point optimized nozzle, designed for a lower pressure difference, still under-expands the flow at the nozzle exit. Conversely, the baseline nozzle experiences reduced over-expansion, mainly due to the increased pressure difference with respect to the design condition, resulting in less intense shock waves downstream compared to the design condition. In this operating condition, a shock-free expansion is achieved for the multi-point optimized nozzle, as the nozzle geometry is adapted to the operating condition.

In off-design C, with the largest pressure difference, the baseline nozzle adapts without shock waves downstream. The multi-point optimized nozzle shows more moderate shock waves than the single-point optimized nozzle, which slightly outperforms it in this scenario.

In summary, the multi-point optimized nozzle displays more moderate shock waves than the baseline in the design condition and outperforms both the single-point optimized and baseline nozzles in off-design A and B. In off-design C, the baseline nozzle excels, but the multi-point optimized nozzle still exhibits slightly less severe shock waves than the single-point optimized nozzle. This suggests that the multi-point optimization strategy, considering a range of operating conditions, allows for better adaptation to the variation of boundary conditions in different cases. It is also crucial to ensure that the optimized nozzle satisfies the mass flow rate constraint for the heat pump cycle, which is essential for maintaining the heating capacity at the desired value. A $\text{WMAPE}_{\text{mass}}$, calculated from Eq. (5), equal to 0.75%, indicates that the multi-point optimized nozzle meets the optimization constraint.

6.2. Impact on system performance

The two-phase nozzle geometries are designed and optimized for use in a Pelton expander, which recovers part of the expansion power lost during throttling from the high pressure of the gas cooler to the low pressure of the evaporator. After obtaining the three nozzle geometries, the mass-weighted average velocity and mass flow rate of the jet are calculated and averaged across five axial locations ($z_i \in [1.1L, 1.2L, \cdots, 1.5L]$), similar to the calculation of nozzle efficiency in Eq. (8). The Pelton wheel geometry remains constant for all nozzles and different working conditions. The extracted power from the Pelton expander is

Table 6
Important cycle parameters during the design and off-design operation of an ASHP.

	$P^t_{in,noz}(bar)$	$T^t_{in,noz}(^\circ C)$	$P_{out,noz}(bar)$	$T_{out,noz}(^\circ C)$	$\dot{m}_{ref}(gs^{-1})$	$n_{comp}(rpm)$
Design	94.2	27.7	37.7	3.0	38.0	5500
Off-design A	89.6	27.7	26.5	−10.0	34.0	7600
Off-design B	124.8	43.5	37.7	3.0	41.3	6200
Off-design C	116.9	43.5	26.5	−10.0	36.7	8600

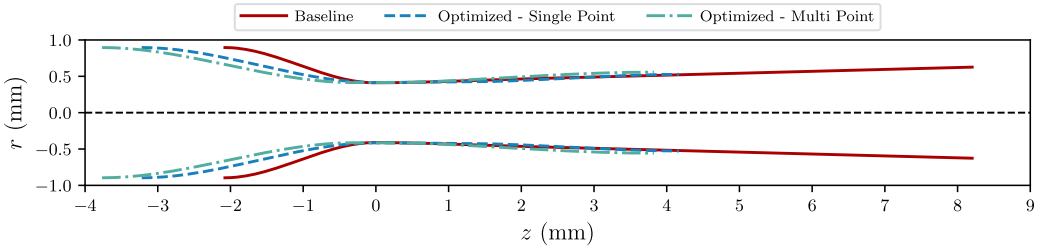

Fig. 14. Geometrical comparison of optimized nozzles, both multi-point and single-point, and baseline nozzle.

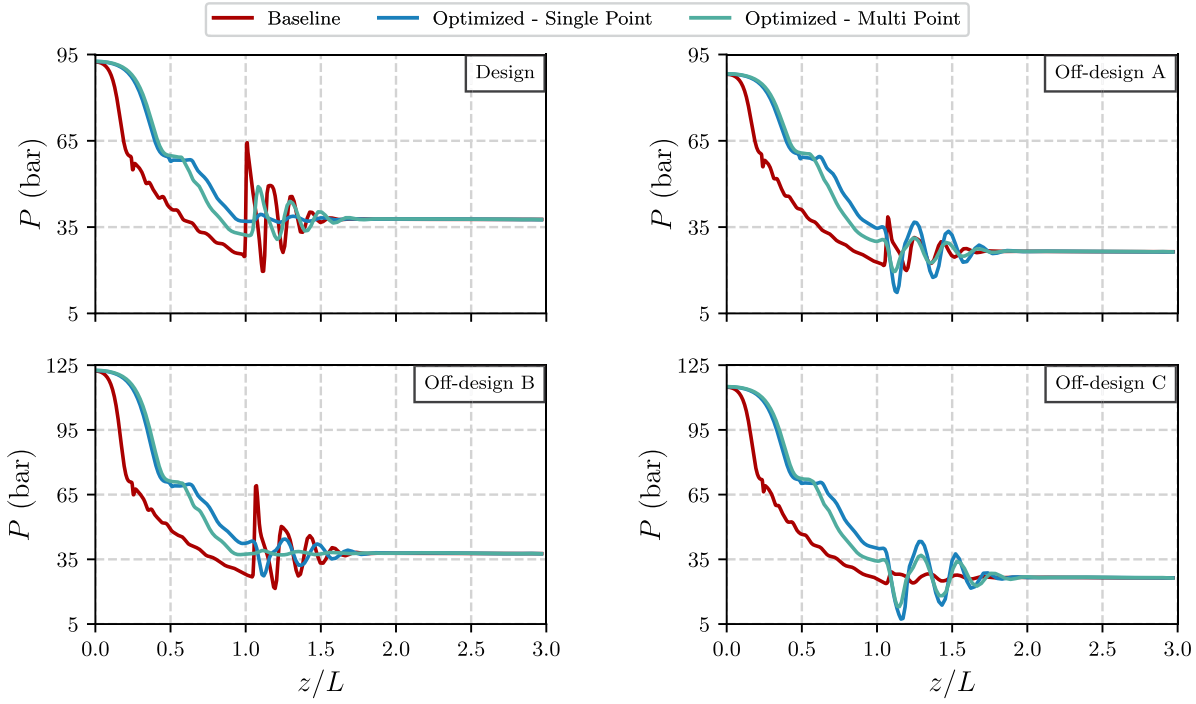

Fig. 15. Pressure along the nozzle axis normalized with respect to the nozzle length along the computational domain for design and off-design conditions, presented for the baseline nozzle, single-point optimized nozzle, and multi-point optimized nozzle.

then calculated at the optimum velocity ratio for each operating condition and each nozzle geometry, $k_p = U/V_{jet}$, where U represents the Pelton wheel peripheral speed, and V_{jet} represents the mass-weighted average velocity of the jet.

The results, including nozzle efficiency, Pelton wheel efficiency, overall expander total-to-static efficiency, and the COP gain of the cycle compared to a cycle with a conventional throttling valve, are presented in Table 7. At the design condition, the multi-point optimized nozzle outperforms the others with a nozzle efficiency of 77.9%. Although the single-point optimized nozzle achieves shock-free expansion, the superior efficiency of the multi-point optimized nozzle is justified because the optimization focuses solely on eliminating shock by minimizing entropy generation along the nozzle axis. However, shear losses and the complex mixing process between the jet and plenum fluid can also impact the overall efficiency evaluation. In practice, when the nozzle discharges into a plenum containing only vapor, the efficiency of the single-point optimized nozzle might surpass that of the multi-point optimized nozzle due to the reduced significance of shear losses, given the lower density of the vapor inside the plenum.

In the off-design A, the baseline nozzle exhibits slightly better performance than the multi-point optimized nozzle. This superiority of the baseline nozzle's performance might be attributed, once again, to the impact of shear losses and mixing inside the plenum, despite the multi-point optimized nozzle having marginally reduced shock waves

Table 7
Performance of the nozzles in design and off-design conditions, along with Pelton wheel and expander efficiency. The COP gain of the ASHP cycle with the expander is also reported.

	Baseline				Single-point optimized				Multi-point optimized			
	η_{noz}(%)	η_{wheel}(%)	η_{exp}(%)	ΔCOP(%)	η_{noz}(%)	η_{wheel}(%)	η_{exp}(%)	ΔCOP(%)	η_{noz}(%)	η_{wheel}(%)	η_{exp}(%)	ΔCOP(%)
Design	66.3	59.5	39.4	6.6	76.2	57.7	43.9	7.4	77.9	57.9	45.1	7.6
Off-design A	76.2	59.4	45.2	7.7	68.9	59.0	40.6	6.8	74.0	59.2	43.8	7.4
Off-design B	73.9	55.3	40.8	9.6	72.4	54.2	39.2	9.2	77.2	55.1	42.5	10.1
Off-design C	77.3	57.2	44.2	10.3	57.7	54.9	31.7	7.2	71.2	56.4	40.1	9.3

compared to the baseline nozzle. In off-design B, the multi-point optimized nozzle outperformed the other nozzles with its shock-free expansion. In off-design C, the baseline nozzle shows the best performance, as expected from its shock-free expansion profile. However, the multi-point nozzle maintains good performance in off-design C compared to the single-point optimized nozzle, achieving 71.2% efficiency compared to 57.7% efficiency for the single-point optimized one.

The nozzle efficiency results highlight the success of multi-point optimization in achieving consistent and efficient performance across various operating conditions by minimizing losses associated with shock waves. The elimination or reduction of shock waves is crucial, especially due to their potential detrimental impact on the Pelton wheel, capable of causing damage to the buckets as well. Additionally, in practical scenarios where the nozzle discharges into a plenum filled only with vapor phase, shear and mixing losses are expected to reduce, thereby affecting the determination of overall efficiency less. Therefore, the focus on reducing shock losses appears to be a reasonable and effective strategy.

The Pelton wheel efficiency remains nearly constant in each operating condition, primarily influenced by windage loss, which depends on factors such as wheel diameter, CO_2 vapor density, and rotational speed. As the rotational speed varies with different nozzles under specific operating conditions, ranging from 64000 rpm to 107000 rpm, the optimum velocity ratio ($k_{p,opt}$) remains almost constant, fluctuating between 0.28 and 0.34. This consistency ensures maintaining a significant share of windage loss relative to the total available power to the wheel. It is worth noting that the efficiency of the Pelton wheel might increase with the reduction of shock waves brought by the multi-point optimization. This reduction leads to a decrease in windage loss as a consequence of the alleviation of droplets scattering around the wheel and more limited shock-bucket interactions. Currently, these effects are not accounted for in the wheel performance estimates, as they are inherently three-dimensional and thus challenging to model through a mean-line approach.

Given the constancy of the wheel efficiency for each operating condition, the expander total-to-static efficiency follows the trend of the nozzle efficiency. Optimizing nozzle performance consequently leads to an optimization of expander performance. The COP of the ASHP cycle with the expander is defined as

$$COP_{exp} = \frac{\dot{Q}_{gc}}{\dot{W}_{comp} - \dot{m}\left(h^{t}_{in,noz} - h^{is}_{out,noz}\right)\eta_{exp}}, \tag{10}$$

where $\dot{W}_{comp}$ is the power consumed by the compressor, and $\left(h^{t}_{in,noz} - h^{is}_{out,noz}\right)$ represents the isentropic total-to-static enthalpy change across the expander. For each operating condition, all terms in Eq. (10) are imposed by the cycle requirements except for η_{exp}. Despite the slight variation in the wheel efficiency of the multi-point optimized case compared to the baseline, the expander efficiency trend mimics that of the nozzle efficiency. From Eq. (10), it is clear that the COP of the heat pump cycle with an expander increases with expander efficiency. Using the multi-point optimized nozzle, the COP of the cycle can be notably increased by an average of 8.6% compared to the cycle with a conventional throttling valve, contributing to the overall efficiency of the ASHP.

7. Conclusion

This paper documents the design strategy for a flashing converging–diverging nozzle intended for use in Pelton turbines, which may replace the conventional throttling valve within domestic heat pump applications. The methodology integrates shape optimization techniques with an in-house homogeneous equilibrium flow model. In order to mitigate the computational cost associated with numerous computational fluid dynamics evaluations, a surrogate strategy employing Kriging responses is adopted. Following an initial training phase composed of 50 Latin hypercube samples, the surrogate prediction undergoes refinement through the acquisition of additional 25 samples via maximization of the constrained expected improvement.

Initially, a single-point optimization is applied to the nozzle to minimize entropy generation at design conditions while constraining the target mass flow rate. This optimization process is repeated 10 times to assess the robustness of the shape optimization method in converging towards the true (global) optimum, irrespective of the initial aleatory design of experiments. Consequently, entropy generation is reduced on average by 98.3%, with a standard deviation of 0.7%, over the ten optimization cases. The examination of the ten optimized profiles reveals an identical diverging section, but variations in the converging sections. This observation confirms that the converging section has marginal effects on nozzle performance.

Following the verification of the shape optimization method, a multi-point shape optimization is conducted, incorporating off-design conditions. The optimization process aims to minimize entropy production across four operating conditions (including the design condition and three off-design conditions), while simultaneously adhering to the mass-flow rate requirements dictated by compressor-expander matching. The off-design conditions are determined through system off-design analysis, which considers variations in the evaporator temperature (due to seasonal temperature changes) and the gas cooler outlet temperature (due to varying user demands). Additionally, a mean-line method is developed for the entire Pelton turbine, integrating results obtained from the nozzle flow simulation with semi-empirical correlations for wheel losses to derive the overall turbine efficiency. Key findings include:

- The optimization effectively yields a geometry that outperforms the baseline design, exhibiting an average nozzle efficiency of 75.1% compared to the baseline efficiency of 73.4% over the four operating conditions. The most notable improvement is observed under design conditions, where the efficiency increases to 77.9% from the baseline value of 66.3%. The optimized geometry incorporates a reduced diverging section and a shorter length, ensuring that downstream shocks do not significantly affect any of the four considered conditions.
- Despite the significant impact of windage loss on the performance of the expander wheel, the improvement in the nozzle design leads to an average 0.5 percentage-point increase in the expander efficiency over the whole operating conditions compared to the baseline geometry. This finding confirms that focusing on the optimization of nozzle aerodynamics is an effective approach to enhancing overall turbine efficiency. However, the combined effects of small-scale effects, shocks, and shear layers contribute to a limited turbine efficiency, which does not exceed 45%.
- Overall, the introduction of the turbine yields significant enhancements to the COP of the heat pump. With regards to the system incorporating the throttling valve, adopting the baseline and the multi-point optimized nozzle geometries leads to COP increases of 6.6% and 7.6%, respectively, under design condition. Thanks to the employed multi-point optimization strategy, this increase in design condition does not compromise off-design performance, which is penalized by a mere 0.3 percentage points over the three considered off-design conditions. The penalty rises to 1.5 percentage points in case the optimization considers only the design condition (single-point formulation).

CRediT authorship contribution statement

Kiavash Kamali: Investigation, Methodology, Software, Validation, Visualization, Writing – original draft, Writing – review & editing. **Paolo Gaetani:** Conceptualization, Methodology, Supervision, Writing – review & editing. **Giacomo Persico:** Methodology. **Alessandro Romei:** Conceptualization, Methodology, Software, Supervision, Visualization,

Writing – original draft, Writing – review & editing.

Declaration of competing interest

The authors declare that they have no known competing financial interests or personal relationships that could have appeared to influence the work reported in this paper.

Data availability

Data will be made available on request.

References

[1] A. Balali, A. Yunusa-Kaltungo, R. Edwards, A systematic review of passive energy consumption optimisation strategy selection for buildings through multiple criteria decision-making techniques, Renew. Sustain. Energy Rev. 171 (2023) 113013, https://doi.org/10.1016/j.rser.2022.113013.

[2] D. Zhang, Y. Ding, Y. Wang, L. Fan, Towards ultra-low energy consumption buildings: Implementation path strategy based on practical effects in China, Energy Sustain. Dev. 70 (2022) 537–548, https://doi.org/10.1016/j.esd.2022.08.025.

[3] J.F. Zhang, Y. Qin, C.C. Wang, Review on CO2 heat pump water heater for residential use in Japan, Renew. Sustain. Energy Rev. 50 (2015) 1383–1391, https://doi.org/10.1016/J.RSER.2015.05.083.

[4] B. Dai, S. Liu, H. Li, Z. Sun, M. Song, Q. Yang, Y. Ma, Energetic performance of transcritical CO2 refrigeration cycles with mechanical subcooling using zeotropic mixture as refrigerant, Energy 150 (2018) 205–221, https://doi.org/10.1016/j.energy.2018.02.111.

[5] M.O. McLinden, C.J. Seeton, A. Pearson, New refrigerants and system configurations for vapor-compression refrigeration, Science 370 (2020) 791–796, https://doi.org/10.1126/science.abe3692.

[6] G. Lorentzen, The use of natural refrigerants: a complete solution to the CFC/HCFC predicament, Int. J. Refrig 18 (1995) 190–197, https://doi.org/10.1016/0140-7007(94)00001-E.

[7] G. Lorentzen, Revival of carbon dioxide as a refrigerant, Int. J. Refrig 17 (1994) 292–301, https://doi.org/10.1016/0140-7007(94)90059-0.

[8] G. Lorentzen, J. Pettersen, A new, efficient and environmentally benign system for car air-conditioning, Int. J. Refrig 16 (1993) 4–12, https://doi.org/10.1016/0140-7007(93)90014-Y.

[9] D.M. Robinson, E.A. Groll, Efficiencies of transcritical CO2 cycles with and without an expansion turbine, Int. J. Refrig 21 (1998) 577–589, https://doi.org/10.1016/S0140-7007(98)00024-3.

[10] S. Elbel, P. Hrnjak, Experimental validation of a prototype ejector designed to reduce throttling losses encountered in transcritical R744 system operation, Int. J. Refrig 31 (2008) 411–422, https://doi.org/10.1016/j.ijrefrig.2007.07.013.

[11] M. Nakagawa, A.R. Marasigan, T. Matsukawa, A. Kurashina, Experimental investigation on the effect of mixing length on the performance of two-phase ejector for CO2 refrigeration cycle with and without heat exchanger, Int. J. Refrig 34 (2011) 1604–1613, https://doi.org/10.1016/j.ijrefrig.2010.07.021.

[12] M. Haida, K. Banasiak, J. Smolka, A. Hafner, T.M. Eikevik, Experimental analysis of the R744 vapour compression rack equipped with the multi-ejector expansion work recovery module, Int. J. Refrig 64 (2016) 93–107, https://doi.org/10.1016/j.ijrefrig.2016.01.017.

[13] T. He, C. Xia, Y. Zhao, L. Li, P. Shu, An Experimental Study on Energy Recovery by a Pelton-Type Expander in a Domestic Refrigeration System, HVAC&R Res 15 (2009) 785–799, https://doi.org/10.1080/10789669.2009.10390864.

[14] M. Okamoto, Development of Two-Phase Flow Expander for CO2 Heat Pumps, in: Short course on 12th Int. Refrig. and Air Con. Conf. at Purdue, West Lafayette, IN, 2008.

[15] N. Stosic, I.K. Smith, A. Kovacevic, A twin screw combined compressor and expander for CO2 refrigeration systems, in: 16th International Compressor Engineering Conference at Purdue, West Lafayette, IN, 2002.

[16] H. Kohsokabe, H. Masaki, K. Hitachi, K. Tojo, H. Appliances, M. Matsunaga, S. Nakayama, M. Koyama, K. Toj0, S.N. Yama, Performance characteristics of scroll expander for CO2 refrigeration cycles, in: International Compressor Engineering Conference at Purdue University, West Lafayette, IN, 2008.

[17] M. Li, Y. Ma, H. Tian, A Rolling Piston-Type Two-Phase Expander in the Transcritical CO2 Cycle, HVAC&R Res 15 (2009) 729–741, https://doi.org/10.1080/10789669.2009.10390860.

[18] J. Nickl, G. Will, H. Quack, W.E. Kraus, Integration of a three-stage expander into a CO2 refrigeration system, Int. J. Refrig 28 (2005) 1219–1224, https://doi.org/10.1016/j.ijrefrig.2005.08.012.

[19] Y. Du, G. Tian, M. Pekris, A comprehensive review of micro-scale expanders for carbon dioxide related power and refrigeration cycles, Appl Therm Eng 201 (2022) 117722, https://doi.org/10.1016/j.applthermaleng.2021.117722.

[20] L. Hays, J.J. Brasz, A transcritical CO2 turbine-compressor, in: International Compressor Engineering Conference at Purdue, West Lafayette, IN, 2004.

[21] C. Corporation, "19XT Hermetic Centrifugal Liquid Chiller", Product Data Form 19XT-1PD, Syracuse, NY, 1995.

[22] E. Tøndell, CO2-expansion work recovery by impulse turbine (Ph.D. thesis), NTNU, (2006). https://ntnuopen.ntnu.no/ntnu-xmlui/handle/11250/233323.

[23] R.E. Henry, H.K. Fauske, The Two-Phase Critical Flow of One-Component Mixtures in Nozzles, Orifices, and Short Tubes, J Heat Transfer 93 (1971) 179–187, https://doi.org/10.1115/1.3449782.

[24] L. Hays, J. Brasz, A Transcritical CO2 Turbine-Compressor, in: International Compressor Engineering Conference (2004). https://docs.lib.purdue.edu/icec/1628.

[25] H. Wang, X. Zhu, Z. Du, Aerodynamic optimization for low pressure turbine exhaust hood using Kriging surrogate model, Int. Commun. Heat Mass Transfer 37 (2010) 998–1003, https://doi.org/10.1016/j.icheatmasstransfer.2010.06.022.

[26] V. Raul, L. Leifsson, Surrogate-based aerodynamic shape optimization for delaying airfoil dynamic stall using Kriging regression and infill criteria, Aerosp Sci Technol 111 (2021) 106555, https://doi.org/10.1016/j.ast.2021.106555.

[27] J. Liu, Z. Han, W. Song, Efficient Kriging-Based Aerodynamic Design of Transonic Airfoils: Some Key Issues, in: 50th AIAA Aerospace Sciences Meeting Including the New Horizons Forum and Aerospace Exposition, American Institute of Aeronautics and Astronautics, Reston, Virigina, 2012. Doi: 10.2514/6.2012-967.

[28] M. Palacz, J. Smolka, A.J. Nowak, K. Banasiak, A. Hafner, Shape optimisation of a two-phase ejector for CO2 refrigeration systems, Int. J. Refrig 74 (2017) 212–223, https://doi.org/10.1016/j.ijrefrig.2016.10.013.

[29] M.S. Lee, H. Lee, Y. Hwang, R. Radermacher, H.-M. Jeong, Optimization of two-phase R600a ejector geometries using a non-equilibrium CFD model, Appl Therm Eng 109 (2016) 272–282, https://doi.org/10.1016/j.applthermaleng.2016.08.078.

[30] R. Span, W. Wagner, A New Equation of State for Carbon Dioxide Covering the Fluid Region from the Triple-Point Temperature to 1100 K at Pressures up to 800 MPa, J Phys Chem Ref Data 25 (1996) 1509–1596, https://doi.org/10.1063/1.555991.

[31] A. Romei, P. Gaetani, G. Persico, Computational fluid-dynamic investigation of a centrifugal compressor with inlet guide vanes for supercritical carbon dioxide power systems, Energy 255 (2022) 124469, https://doi.org/10.1016/j.energy.2022.124469.

[32] M. Nakagawa, M.S. Berana, A. Kishine, Supersonic two-phase flow of CO2 through converging–diverging nozzles for the ejector refrigeration cycle, Int. J. Refrig 32 (2009) 1195–1202, https://doi.org/10.1016/j.ijrefrig.2009.01.015.

[33] A.I.J. Forrester, A.J. Keane, N.W. Bressloff, Design and Analysis of "Noisy" Computer Experiments, AIAA J. 44 (2006) 2331–2339, https://doi.org/10.2514/1.20068.

[34] W.J. Sacks, T.J. Welch, H.W. Mitchell, Design and analysis of computer experiments, Stat. Sci. (1989) 409–453.

[35] T.W. Simpson, J.D. Peplinski, P.N. Koch, J.K. Allen, Metamodels for computer-based engineering design: Survey and recommendations, Eng Comput 17 (2001) 129–150, https://doi.org/10.1007/PL00007198.

[36] B. Matérn, Spatial variation, Springer Science & Business Media, 2013.

[37] D.R. Jones, M. Schonlau, W.J. Welch, Efficient Global Optimization of Expensive Black-Box Functions, J. Glob. Optim. 13 (1998) 455–492, https://doi.org/10.1023/A:1008306431147.

[38] A. Forrester, A. Sobester, A. Keane, Engineering design via surrogate modelling: a practical guide, John Wiley & Sons, Wiltshire, Great Britain, 2008.

[39] R. Storn, K. Price, Differential Evolution - A Simple and Efficient Heuristic for Global Optimization over Continuous Spaces, J. Glob. Optim. 11 (1997) 341–359, https://doi.org/10.1023/A:1008202821328.

[40] P. Virtanen, R. Gommers, T.E. Oliphant, M. Haberland, T. Reddy, D. Cournapeau, E. Burovski, P. Peterson, W. Weckesser, J. Bright, et al., SciPy 1.0: fundamental algorithms for scientific computing in Python, Nat Methods 17 (2020) 261–272. Doi: 10.1038/s41592-019-0686-2.

[41] J. Liu, Z. Han, Song. W, Comparison of infill sampling criteria in kriging-based aerodynamic optimization, in: 28th Congress of the International Council of the Aeronautical Sciences, 2012: pp. 1625–1634.

[42] Z. Chen, G. Liu, H. Zhao, J. Deng, Analysis of the internal flow features of a CO2 transonic nozzle and optimization of the nozzle shape profile, Appl Therm Eng 238 (2024) 121945, https://doi.org/10.1016/j.applthermaleng.2023.121945.

[43] J.M. Smith, H.C. Van Ness, M.M. Abbott, M.T. Swihart, Introduction to chemical engineering thermodynamics, McGraw-Hill, Singapore, 1949.

[44] C. Lettieri, D. Paxson, Z. Spakovszky, P. Bryanston-Cross, Characterization of Nonequilibrium Condensation of Supercritical Carbon Dioxide in a de Laval Nozzle, J Eng Gas Turbine Power 140 (2018), https://doi.org/10.1115/1.4038082.

[45] L. Geng, H. Liu, X. Wei, CFD analysis of the flashing flow characteristics of subcritical refrigerant R134a through converging-diverging nozzles, Int. J. Therm. Sci. 137 (2019) 438–445, https://doi.org/10.1016/j.ijthermalsci.2018.12.011.

[46] J.D. Anderson, Modern compressible flow: with historical perspective (Vol. 12), McGraw-Hill, New York, 1990.

[47] G. Farin, Curves and Surfaces for Computer Aided Design, A Practical Guide, fifth ed., CA, USA, San Francisco, 2002.

[48] R. Cabello, D. Sánchez, R. Llopis, E. Torrella, Experimental evaluation of the energy efficiency of a CO2 refrigerating plant working in transcritical conditions, Appl Therm Eng 28 (2008) 1596–1604, https://doi.org/10.1016/J.APPLTHERMALENG.2007.10.026.

[49] Q. Cui, D. Wei, E. Gao, X. Zhang, Compressor control strategy for CO2 heat pump toward efficient and stable domestic hot water production: An experimental investigation, Thermal Science and Engineering Progress 38 (2023) 101681, https://doi.org/10.1016/J.TSEP.2023.101681.

[50] Y. Yang, X. Peng, G. Wang, X. Liu, D. Wang, Energetic and exergetic analysis of a transcritical CO2 air-source heat pump water heating system in the cold region, Energy Build 298 (2023) 113558, https://doi.org/10.1016/J.ENBUILD.2023.113558.

[51] L.F. Richardson, J.A. Gaunt, VIII. The deferred approach to the limit, Philosophical Transactions of the Royal Society of London. Series A, Containing Papers of a

Mathematical or Physical Character 226 (1927) 299–361. Doi: 10.1098/rsta.1927.0008.
[52] L.F. Richardson, IX. The approximate arithmetical solution by finite differences of physical problems involving differential equations, with an application to the stresses in a masonry dam, Philosophical Transactions of the Royal Society of London. Series A, Containing Papers of a Mathematical or Physical Character 210 (1911) 307–357. Doi: 10.1098/rsta.1911.0009.
[53] I.B. Celik, U. Ghia, P.J. Roache, C.J. Freitas, Procedure for Estimation and Reporting of Uncertainty Due to Discretization in CFD Applications, J Fluids Eng 130 (2008) 078001, https://doi.org/10.1115/1.2960953.
[54] M.D. McKay, R.J. Beckman, W.J. Conover, A comparison of three methods for selecting values of input variables in the analysis of output from a computer code, Technometrics 42 (2000) 55–61, https://doi.org/10.1080/00401706.2000.10485979.
[55] J. Zhu, S. Elbel, CFD simulation of vortex flashing R134a flow expanded through convergent-divergent nozzles, Int. J. Refrig 112 (2020) 56–68, https://doi.org/10.1016/j.ijrefrig.2019.12.005.
[56] Z. Zhang, Pelton Turbines, Springer International Publishing, Cham (2016), https://doi.org/10.1007/978-3-319-31909-4.
[57] S. Minetto, Theoretical and experimental analysis of a CO2 heat pump for domestic hot water, Int. J. Refrig 34 (2011) 742–751, https://doi.org/10.1016/j.ijrefrig.2010.12.018.
[58] Z. Wang, F. Wang, G. Li, M. Song, Z. Ma, H. Ren, K. Li, Experimental investigation on thermal characteristics of transcritical CO2 heat pump unit combined with thermal energy storage for residential heating, Appl Therm Eng 165 (2020), https://doi.org/10.1016/J.APPLTHERMALENG.2019.114505.
[59] S.M. Liao, T.S. Zhao, A. Jakobsen, A correlation of optimal heat rejection pressures in transcritical carbon dioxide cycles, Appl Therm Eng 20 (2000) 831–841, https://doi.org/10.1016/S1359-4311(99)00070-8.